



Experimental demonstration of a dissipative multi-resonator metamaterial for broadband elastic wave attenuation

Miles V. Barnhart^a, Xianchen Xu^a, Yangyang Chen^{a, **}, Shun Zhang^b,
Jizhou Song^b, Guoliang Huang^{a, *}

^a Department of Mechanical and Aerospace Engineering, University of Missouri, Columbia, MO 65211, USA

^b Department of Engineering Mechanics and Soft Matter Research Center, Zhejiang University, Hangzhou 310027, China

ARTICLE INFO

Article history:

Received 17 April 2018
Received in revised form 28 July 2018
Accepted 16 August 2018
Available online 10 September 2018
Handling Editor: Erasmo Carrera

Keywords:

Dissipative elastic metamaterials
Broadband energy attenuation
Microstructural design

ABSTRACT

Elastic metamaterials (EMMs) encompass a relatively new class of composite materials that exhibit unique dynamic effective material properties and possess the ability to mitigate or even completely inhibit the propagation of acoustic/elastic waves over specific frequency spectrums (band gaps). However, it is extremely difficult to achieve broadband energy absorption with single resonance based EMMs. Dissipative EMMs with multiple resonators have recently been suggested for the attenuation of elastic wave energy spanning broad frequency spectrums. In this study, we fabricate a dissipative EMM with multiple resonators comprised from layered spherical inclusions embedded in an epoxy matrix and experimentally demonstrate broadband elastic wave mitigation. An analytical solution combined with numerical simulations is used to validate the accuracy of the fabrication based on a single unit cell test. We also numerically investigate the dynamic wave dispersion behavior of the fabricated dissipative EMM and find that the two strong attenuation regions induced by the two internal resonators can be effectively combined into a broadband wave attenuation region by the intrinsic damping properties of the constitutive materials used in the design. This broadband wave attenuation is finally demonstrated through an impact test performed on finite EMM samples where the frequency spectrum of the transmitted amplitude is in very good agreement with the numerical results. This design can be easily scaled and implemented into different length scales, which will benefit a range of applications requiring broadband vibration, elastic wave, and/or seismic wave mitigation.

© 2018 Elsevier Ltd. All rights reserved.

1. Introduction

Metamaterials comprise a relatively new field of composites research which derive their unique effective material properties from a specially engineered microstructure rather than the conventional materials used in their fabrication. These non-naturally occurring material properties were first considered in the field of electromagnetics in which the possibility of a material possessing simultaneously negative permittivity, ϵ , and permeability, μ , was proposed [1]. Analogous to their

* Corresponding author.

** Corresponding author.

E-mail addresses: yc896@mail.missouri.edu (Y. Chen), huangg@missouri.edu (G. Huang).

electromagnetic counterparts, acoustic/elastic metamaterials (EMMs) have more recently been explored [2] for their applications including blast wave mitigation [3], seismic wave protection [4], enhanced flexural wave sensing [5] and many other applications involving the manipulation of elastic/acoustic wave propagation. By specially designing substructures in single- or multi-phase materials, a locally resonant mechanism can be created to allow frequency dependent effective material properties. Based on this local resonance concept, EMMs are capable of exhibiting frequency band gap regions, or, regions in which the propagation of acoustic and/or elastic waves is prohibited. Methods to widen these regions have been proposed for phononic crystals where it has been numerically demonstrated that the band gaps formed by Bragg scattering and local resonance can be combined to achieve wider band gap regions [6–8]. The first experimental demonstration of a locally resonant acoustic metamaterial was carried out by Liu et al. [9], in which locally resonant unit cells consisting of lead (Pb) spheres coated with a compliant silicone rubber were arranged periodically in an epoxy matrix. It was experimentally demonstrated that the effective medium produced strong sound attenuation regions restricting the transmission of incident acoustic waves. More recently, locally resonant granular chains constructed with internal resonators have been used to experimentally demonstrate elastic wave band gap behavior [10].

Although the local resonance mechanism exhibited by EMMs has been extensively studied, it was not until recently that the effects of damping on the dynamic behavior and overall effective energy attenuation was considered [3,11–16]. This phenomenon, termed “metadamping”, can help to address a key weakness of conventional non-dissipative EMM microstructural designs where the band gap region(s) are usually relatively narrow and only present near the local resonance frequency of the microstructure. By including dissipative properties into a conventional multi-resonator EMM microstructural design [17–19], it was numerically demonstrated that the two band gap regions could be effectively merged into a single broadband absorption region by carefully selecting the dissipative parameters [3]. This means that broadband energy absorption can be achieved without the need to adjust the local resonant frequency of the EMM microstructure, which would require physical modification and is therefore unrealistic.

Here, we propose an EMM microstructure design capable of energy absorption over a broad range of frequencies by incorporating dissipative constituent materials in the metamaterials microstructure. The goal of this work is to experimentally validate the metadamping concept for a multi-resonator EMM unit cell design comprised from five constituent materials with highly contrasting material properties making their arrangement equivalent to mass-spring-damper components. Experimental analysis is conducted to measure the dynamic response of a single multi-resonator unit cell. The experimentally measured frequency response is then compared with those obtained from analytical modeling. Investigation of the multi-resonator unit cell band structure and wave attenuation properties over a frequency range of 0 kHz–8 kHz is then carried out via dispersion relations obtained from numerical modeling using the finite element method. Finally, experimental transmission testing is conducted for lattices consisting of five and ten unit cells to demonstrate the broadband energy attenuation mechanism and compared with the numerical results.

2. Multi-resonator metamaterial design and fabrication

The final microstructural design was influenced by two key parameters. The first is the previous obtained results from numerical modeling of a dissipative multi-resonator microstructure with respect to the broadband wave attenuation performance. The second was based on the commercially available lead (Pb) sheet thicknesses to allow for in-house forming of the relatively “soft” hemispherical metal layers. The final design geometry is illustrated in Fig. 1, where a 4 mm diameter

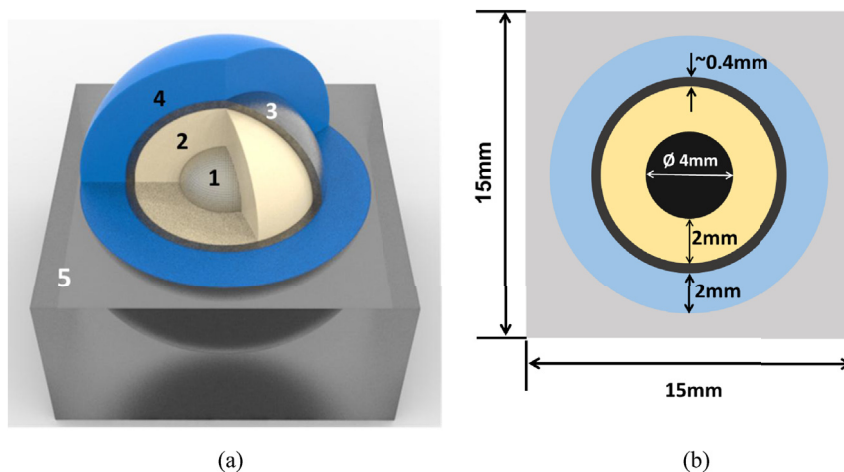


Fig. 1. Multi-resonator unit cell (a) three-dimensional rendering where material 1 = 4 mm diameter tungsten sphere, material 2 = 2 mm thick urethane rubber coating, material 3 = 0.4 mm thick lead-mass layer, material 4 = 2 mm thick silicone rubber coating, material 5 = rigid epoxy matrix and (b) cross-section with geometric parameters.

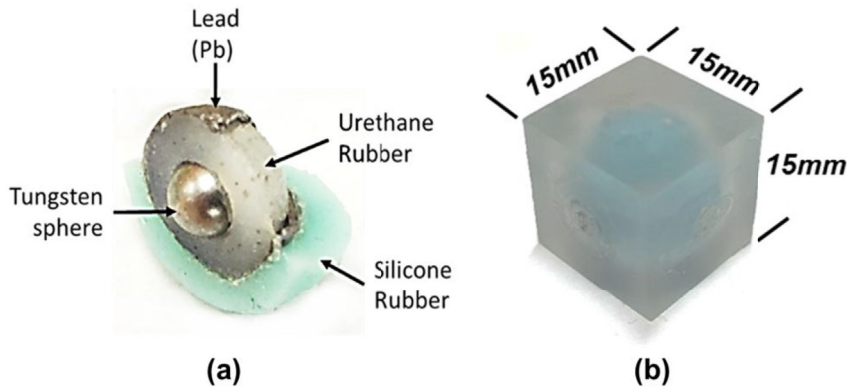


Fig. 2. Fabricated multi-resonator unit cell used in experimental analysis (a) cross section of fabricated unit cell and (b) final fabricated unit cell embedded within epoxy matrix.

spherical tungsten core coated with a 2 mm thick layer of urethane rubber is encapsulated by a 0.4 mm thick layer of lead (Pb) coated with a 2 mm thick layer of silicone rubber. The layered spherical inclusion is finally embedded within an epoxy matrix with a lattice constant of 15 mm. For clarity, an illustrative rendering as well as a cross-section of the final multi-resonator unit cell with geometric parameters are shown in Fig. 1(a) and (b), respectively.

To realize a physical multi-resonator metamaterial structure, more recent as well as traditional manufacturing methods were employed including three-dimensional (3D) printing, “room-temperature” injection molding and metal stamping/pressing. The initial step involved coating 4 mm diameter tungsten spheres with a 2 mm thick coat of Simpack® 60A urethane rubber using 3D printed molds designed to coat the spheres one side at a time. Once the innermost tungsten core was fully coated, two 0.4 mm thick hemispherical shells of lead were attached with superglue to fully encapsulate the urethane-tungsten structure. The hemispherical lead shells were fabricated by stamping disks from a piece of lead sheet before pressing the disks into a hemispherical shape using a specially machined tool and die. The outer silicone rubber (Mold Star® 16A FAST) layer was added using the same technique used for the inner urethane rubber coating and slightly larger 3D printed molds. The final unit cells (shown in Fig. 2(b)) were then embedded within a rigid epoxy matrix of EpoxAcast® 690 using specially fabricated molds. For a comprehensive step-by-step outline of the unit fabrication process, please see [section S.1 in the Supplementary Materials](#).

3. Experimental setup and testing

Two experimental approaches were used to demonstrate the dynamic properties of the multi-resonator metamaterial design. The first method was to measure the frequency responses of a single multi-resonator unit cell using an LDS® 201 permanent magnet shaker as the excitation source with an accelerometer (Bruel & Kjaer Type 4516) mounted on the top of the sample as shown in Fig. 3 below. The shaker was fixed to an optical table (Thorlabs T48H) to insure isolation from outside disturbances during experimental measurements. In the single unit cell experimental testing, a white noise excitation signal

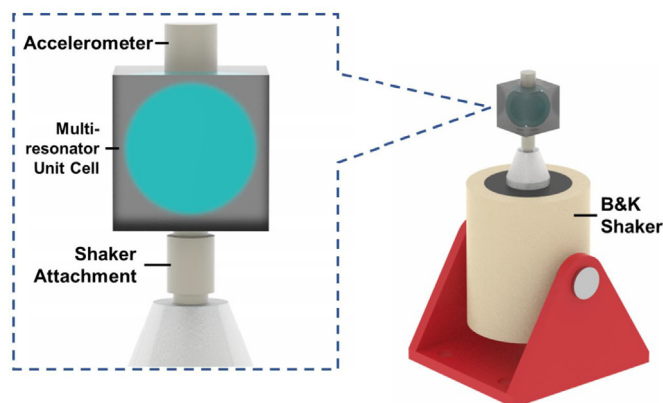


Fig. 3. Experimental setup used to measure individual unit cell responses.

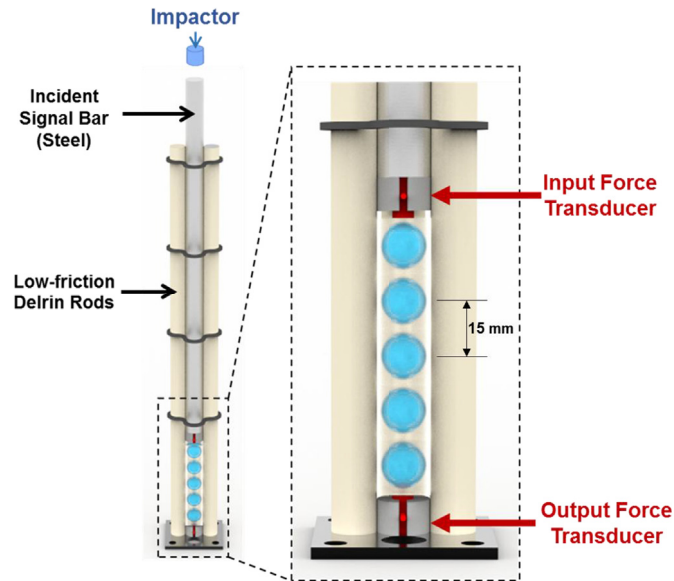


Fig. 4. Experimental setup used to measure transmission coefficient under impact excitation.

was generated using a Bruel & Kjaer PHOTON + dynamic signal analyzer and then amplified with a LDS PA25E power amplifier which drives the shaker excitation signal over the frequency range of 0 kHz–8 kHz.

The second experimental approach shown in Fig. 4 was used to measure the transmission properties through a finite lattice of multi-resonator unit cells embedded within a rigid epoxy block. It should be noted that this experimental design was inspired by previously presented work investigating the transmission of elastic waves through locally resonant metamaterial and phononic crystal lattices [10,20–24]. Four low friction Delrin rods were used to constrain the displacement to a single direction. Two piezoelectric force transducers attached to the two sides of the sample were used to measure the input and transmitted signals through an empty epoxy block and five- and ten-unit cell multi-resonator lattices. A 1 ft (0.3048 m) steel rod with a diameter of 15 mm was placed on top of the lattice specimen to act as an incident signal bar. It should be noted that a 15 mm diameter brace for the piezoelectric force transducer were also fabricated using 3D printing to ensure that measurements were limited to a single direction.

4. Results

4.1. Validation of fabrication

Our initial analysis is to validate the accuracy of the fabricated unit cell by comparing the experimental frequency response of a single multi-resonator unit cell to the response obtained from an analytical model. To obtain the stiffness and damping properties (storage and loss modulus) used in analytical and later numerical modeling, dynamic material analysis (DMA) was conducted using multiple physical material samples of the silicone rubber, urethane rubber and epoxy resin materials used in the construction of the unit cells (ASTM D4065, D4440, D5279). Examples of the results obtained from DMA testing can be found in the [S.2 Supplementary Materials](#) which were each tested at 150 Hz. Another benefit of conducting the DMA testing for the elastomers and epoxy used in the experimental specimen construction is to obtain accurate damping properties of the real materials. This is given by the ratio between the loss modulus and storage modulus of the material to compute the loss coefficients of each material used in the unit cell construction. The loss coefficients used in the following analytical modeling for the silicone and urethane rubbers components are given as $\eta_2 = \eta_{\text{silicone}} = 0.12$ and $\eta_3 = \eta_{\text{urethane}} = 0.25$, respectively.

To approximate the stiffness parameters that will be used in the analytical frequency response analysis, the commercial finite element software COMSOL Multiphysics is employed to conduct 3D eigenfrequency analysis. In the 3D numerical

Table 1
Material parameters used in numerical simulations.

	Epoxy	Lead	Tungsten	Silicone Rubber	Urethane Rubber
Modulus of Elasticity, E (GPa)	3.0	16.0	410.0	0.00265	0.004
Poisson's Ratio, ν	0.33	0.4	0.28	0.49	0.49
Density, ρ (kg/m ³)	1100	11350	17500	1000	1000

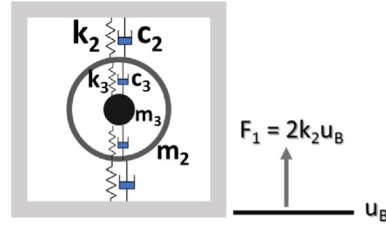


Fig. 5. Analogous mass-spring-damper representation of multi-resonator unit cell.

eigenfrequency study, the material parameters for the Young's moduli (neglecting damping) were defined as those obtained from DMA testing while the densities were directly measured using weight-to-volume ratios which are listed in Table 1. The resonant frequencies for the two longitudinal modes of the multi-resonator unit cell are calculated and shown in Fig. 6, where the corresponding mode shapes are also illustrated. The spring-stiffness parameters can be approximated by fitting the resonant frequencies of the lumped model with the values obtained numerically. We begin to formulate our analytical model by considering an analogous mass-spring system shown in Fig. 5, where the stiffness coefficients k_2 and k_3 , and damping coefficients c_2 and c_3 , represent the outer 2 mm thick silicone rubber coating and the innermost 2 mm thick urethane rubber coating, respectively. Similarly, the masses m_2 and m_3 denote hemispherical lead layer and inner-most spherical tungsten mass, respectively.

The undamped equations of motion for the system can then be readily obtained as

$$m_B \ddot{u}_B + 2k_2[u_B - u_2] = f_r \quad (1a)$$

$$m_2 \ddot{u}_2 - 2u_B k_2 + 2u_2[k_2 + k_3] - 2u_3 k_3 = 0, \quad (1b)$$

$$m_3 \ddot{u}_3 + 2k_3[u_3 - u_2] = 0, \quad (1c)$$

where u_B , u_2 and u_3 represent the displacements of the epoxy matrix base, middle mass and innermost mass, respectively, and f_r denotes the excitation force.

Taking the harmonic solution for the displacements given in Eq. (1), the system of equations can be rewritten in a matrix form as

$$-\omega^2 \begin{bmatrix} m_B & 0 & 0 \\ 0 & m_2 & 0 \\ 0 & 0 & m_3 \end{bmatrix} \begin{pmatrix} U_B \\ U_2 \\ U_3 \end{pmatrix} + \begin{bmatrix} 2k_2 & -2k_2 & 0 \\ -2k_2 & 2(k_2 + k_3) & -2k_3 \\ 0 & -2k_3 & 2k_3 \end{bmatrix} \begin{pmatrix} U_B \\ U_2 \\ U_3 \end{pmatrix} = \begin{pmatrix} F_r \\ 0 \\ 0 \end{pmatrix}, \quad (2)$$

where U_B , U_2 , U_3 and F_r are the complex amplitudes of the displacements corresponding to each of the three rigid bodies and the excitation force. By imposing $U_B = 0$, the two local resonant frequencies can be obtained by solving the resulting system of equations given as

$$\begin{vmatrix} -\omega^2 m_2 + 2(k_2 + k_3) & -2k_3 \\ -2k_3 & -\omega^2 m_3 + 2k_3 \end{vmatrix} = 0. \quad (3)$$

The mass values were directly measured as $m_B \approx 2.5$ g, $m_2 \approx 1$ g and $m_3 \approx 0.6$ g. Letting $\omega_1 = 2\pi f_{n,1}$, and $\omega_2 = 2\pi f_{n,2}$, the spring stiffnesses k_2 and k_3 can be determined. Finally, the approximate stiffness parameters and known mass parameters are listed in Table 2, which can be used to validate the unit cell fabrication analytically based on single unit cell dynamic tests.

To analytically model the multi-resonator unit cell shown in Fig. 1(b), an analogous mass-spring-damper system is considered as shown in Fig. 5. The equations of motion for the three degree-of-freedom (3-DOF) unit cell can be written as

$$\mathbf{M} \frac{\partial^2 \bar{\mathbf{u}}}{\partial t^2} + \mathbf{K} \bar{\mathbf{u}} = \mathbf{F}, \quad (4)$$

where

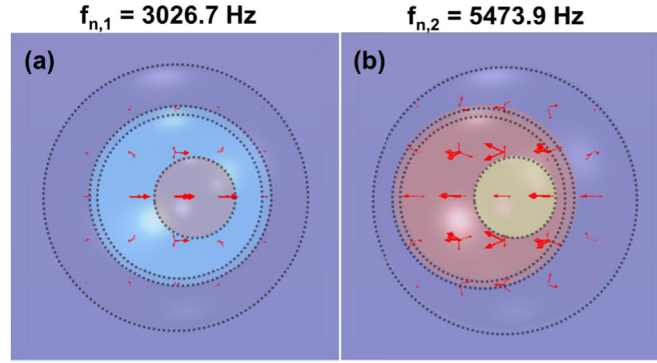


Fig. 6. Numerically obtained multi-resonator unit cell mode shapes (longitudinal).

Table 2

Mass and stiffness parameters used for analytical modeling.

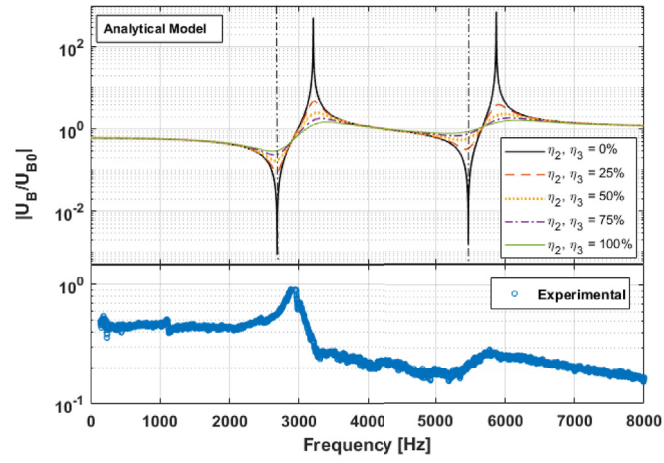
Continuum media	Outer epoxy block	Lead (Pb) hemispherical layer	4 mm diameter tungsten sphere	2 mm thick silicone rubber layer	2 mm thick urethane rubber layer
Mass-spring analogy	m_B	m_2	m_3	k_2	k_3
	2.5	1.0	0.6	3.7675×10^5	1.3509×10^5

$$\begin{aligned}
 \mathbf{M} &= \begin{bmatrix} m_B & 0 & 0 \\ 0 & m_2 & 0 \\ 0 & 0 & m_3 \end{bmatrix}, \\
 \mathbf{K} &= \begin{bmatrix} 2k_2(1 + i\eta_2) & -2k_2(1 + i\eta_2) & 0 \\ -2k_2(1 + i\eta_2) & 2[k_2(1 + i\eta_2) + k_3(1 + i\eta_3)] & -2k_3(1 + i\eta_3) \\ 0 & -2k_3(1 + i\eta_3) & 2k_3(1 + i\eta_3) \end{bmatrix}, \\
 \mathbf{F} &= \begin{pmatrix} F_A \\ 0 \\ 0 \end{pmatrix}, \quad \bar{\mathbf{u}} = \begin{pmatrix} U_B \\ U_2 \\ U_3 \end{pmatrix}, \quad \eta_2 = \frac{\omega c_2}{k_2}, \eta_3 = \frac{\omega c_3}{k_3},
 \end{aligned} \tag{5}$$

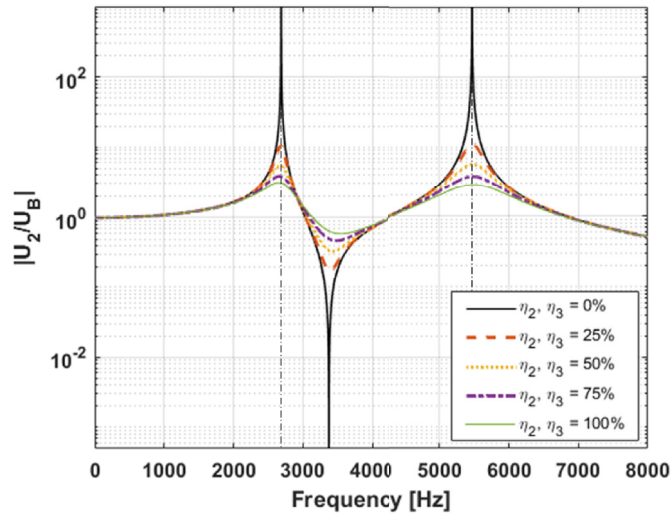
and F_A is the applied force on the base.

Analytically calculated frequency responses of mass displacement amplitudes are shown in Fig. 7(a)–(c). It should be noted that the resulting displacement of the outermost mass (U_B) is normalized with respect to the displacement amplitude of an empty block case where $u_{B0} = 1/m_B\omega^2$. Along with the mass and stiffness parameters listed in Table 2, the material damping properties obtained from DMA testing are included in the stiffness matrix as imaginary coefficients with different degrees of damping amplitude shown in the response curves.

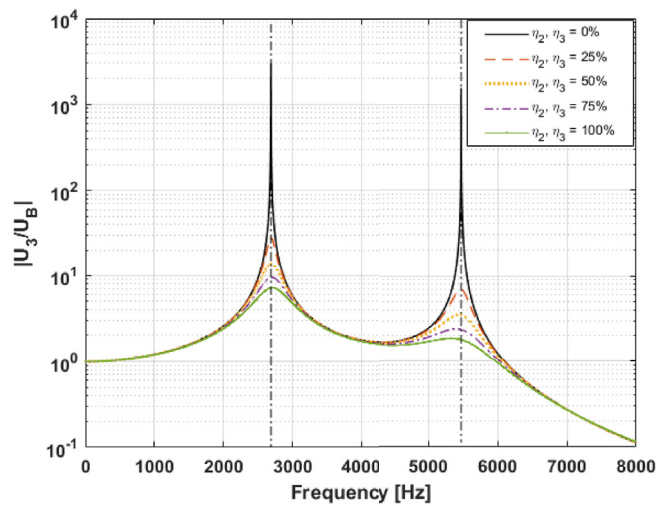
In the top of Fig. 7(a), two zero-displacement dips of the outer epoxy block (U_B) are clearly visible at ~2700 Hz and ~5500 Hz which correspond to the two resonant frequencies of the internal masses (m_2 and m_3) denoted by the displacement peaks shown Fig. 7(b) and (c). As the damping is gradually increased in the system to 100% ($\eta_2 = 0.12$, and $\eta_3 = 0.25$), it is clear in Fig. 7(a) that the response peaks and dips of the outer epoxy block are significantly suppressed. This is also apparent in the experimentally measured response shown in the bottom of Fig. 7(a) which shows reasonable agreement with the analytically obtained displacement curve. As the damping coefficients are gradually increased we see that the dips and peaks becomes increasingly weak and nearly flat for the experimental damping coefficient values. This makes experimental observations extremely difficult, as it is not possible to adjust the damping coefficients in the experimental case. Therefore, it is not surprising that the experimental results in Fig. 7 do not have clear dip-and-peak features due to the strong internal damping properties.



(a)



(b)



(c)

Fig. 7. (a) Comparison between analytically obtained (top - solid black line) and experimentally measured (bottom - blue circles) frequency responses, (b) analytically obtained displacement field of middle mass (m_2) and (c) innermost mass (m_3). Analytically obtained resonant frequencies are denoted by dash-dotted vertical lines. (For interpretation of the references to colour in this figure legend, the reader is referred to the Web version of this article.)

4.2. One-dimensional dispersion and transmission analyses using the finite element method

For the first numerical analyses, a 2D $\kappa(\omega)$ approach [3,25] is used to obtain the dispersion relations for periodic meta-materials of non-dissipative and dissipative multi-resonator unit cells using the commercial software COMSOL Multiphysics. It should be noted that, although the interior components of the final multi-resonator unit cell have a spherical geometry and the exterior of the unit cell is a block, it has been previously demonstrated that the band structures for a 3D geometry and simplified 2D axial-symmetric geometry are nearly identical [26]. In the final numerical study, the frequency domain transmission amplitudes for a finite lattice is calculated for comparison with dispersion relations and experimentally measured transmission amplitudes of finite lattices consisting of five and ten multi-resonator unit cells.

Using the material properties listed in Table 1 to represent the continuum materials in a multi-resonator unit cell, the band structure for a unit cell (without damping considered) is numerically obtained using the $\kappa(\omega)$ approach as shown in Fig. 8(a). In the figure, the low frequency acoustic branch and two higher frequency optical branches are separated by two distinct band gap regions. The first band gap spans the frequency region of ~ 2.5 kHz– ~ 3.7 kHz while the second higher frequency region is from ~ 5.9 kHz to ~ 6.6 kHz.

To consider the material damping properties in the numerical dispersion analysis, the dispersion bands are obtained by solving for the complex wavenumber bands over the first irreducible Brillouin zone [27] of a single multi-resonator unit cell

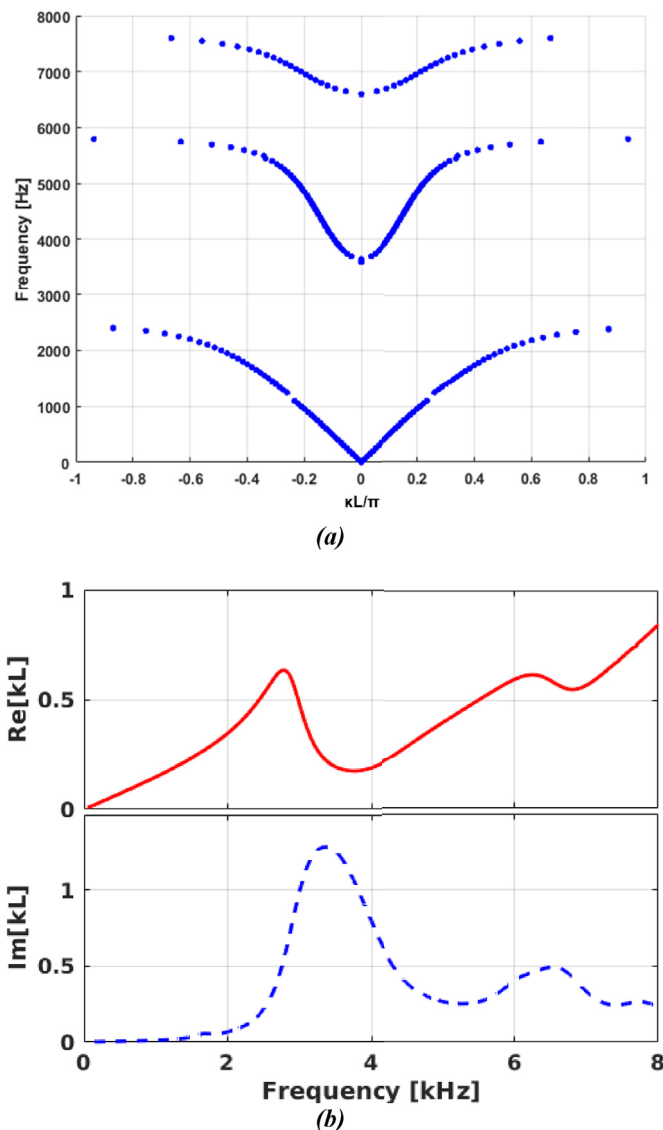
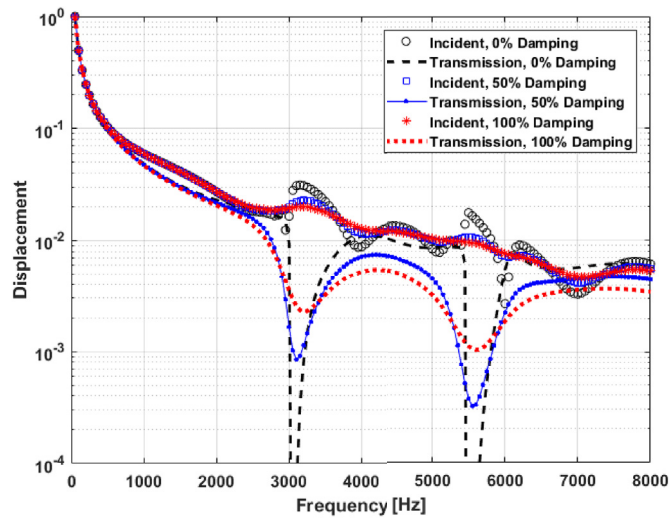


Fig. 8. Calculated band structure using 2D finite element method and $\kappa(\omega)$ approach for (a) undamped multi-resonator structure and (b) multi-resonator structure with damping applied.

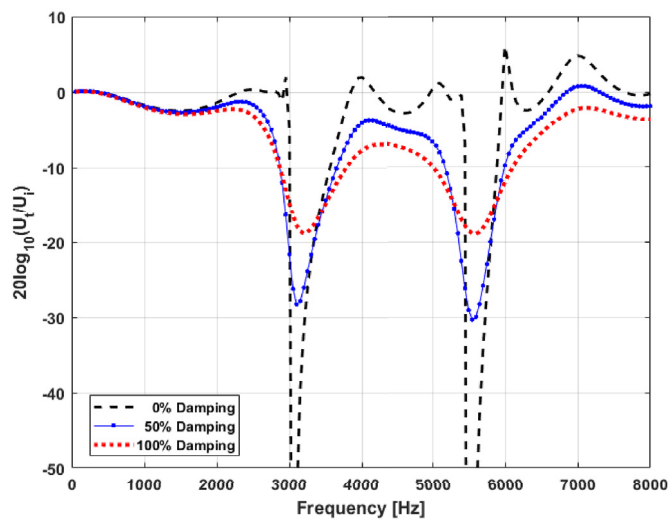
by sweeping the frequency, ω . In the study, realistic damping parameters for the epoxy, silicone rubber and urethane rubber are defined as those obtained from the DMA tests. Using this approach, the real and imaginary components of the complex wavenumber are obtained as shown in Fig. 8(b). In the top portion of the figure, the real part of the complex wavenumber is shown and corresponds to the propagation factor while in the bottom the imaginary component of the complex wavenumber denotes the attenuation factor through a periodic lattice. It should be noted that, with the addition of material damping in the



Fig. 9. 2D numerical model of finite lattice of multi-resonator unit cells embedded within a rigid epoxy matrix.



(a)



(b)

Fig. 10. Numerically obtained comparison of transmission amplitudes of ten unit cell finite lattice with different damping values for (a) displacement values at incident and transmission boundaries and (b) magnitude (dB) of transmitted signal.

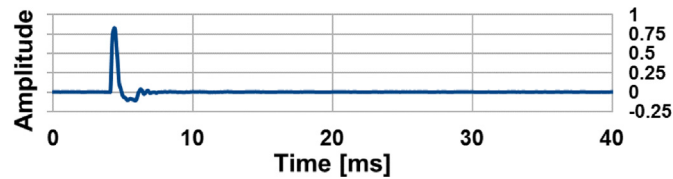


Fig. 11. Experimental input signal from impact excitation in the time domain (measured from first piezo force transducer).

unit cell microstructure, pure band gap regions will no longer be present in the wavenumber dispersion bands. By incorporating material damping properties within the microstructural design, it is now possible to produce a broad attenuation region denoted by the imaginary component of the complex wavenumber which is no longer limited/fixed to specific frequency regions near resonances.

For the final numerical analysis, the transmitted wave amplitudes from a finite metamaterial of ten unit cells embedded within a rigid epoxy matrix are numerically calculated using a 2D frequency domain study. In the 2D numerical model shown in Fig. 9, the upper boundaries (outer) are modelled with a roller boundary condition to simulate the 1D displacement constraint imposed on the experimental lattice by the four Delrin[®] guide rods, and lower boundaries are at the symmetric axis. Perfectly matched layers (PMLs) are modelled on each side of the lattice and two probes are used to measure the incident and transmitted signals at equal distances from the first and last unit cell of the lattice, respectively. A prescribed boundary force is applied normal to the left vertical boundary of the incident domain. It should be noted that, in the 2D axisymmetric numerical model, the incident and transmission domains were modelled with longer geometries but were truncated to provide a clearer final figure of the geometry.

To demonstrate the influence of damping on the overall attenuation performance of the finite lattice, numerical analysis with 50% and 100% damping values are compared with a zero-damping case as shown in Fig. 10(a) and (b). The displacement amplitudes obtained from the incident and transmission point probes are illustrated in Fig. 10(a) where two distinct dips are apparent for each of the three cases in the transmission probe amplitude near the two natural frequencies previously shown in Fig. 6 (3026.7 Hz and 5473.9 Hz). It can also be clearly seen in the transmission ratio shown in Fig. 10(b) that the two distinct dips are effectively joined as the degree of damping increases, generating a broad wave attenuation region. These results for the finite lattice structure with different degrees of damping considered are also in good agreement with the frequency region of the non-zero imaginary part of the wavenumber shown in Fig. 8. However, it should be noted that although a single broad attenuation region can be produced by increasing the degree of damping in the system, the attenuation amplitude near the two resonant frequencies is significantly decreased. This is due to the fact that as the internal damping parameters are increased, the locally resonant motions of the two resonant inclusions are inhibited [3]. In the final section, we will provide experimentally measured transmission amplitudes for a finite lattice consisting of five and ten unit cells to further validate the design for broadband wave mitigation.

4.3. Experimental demonstration of broadband wave mitigation

The experimental excitation force was generated using a small metal rod dropped from a prescribed and repeatable height without allowing multiple impacts due to the impactor “bouncing” on the steel incidence bar. The force amplitudes are

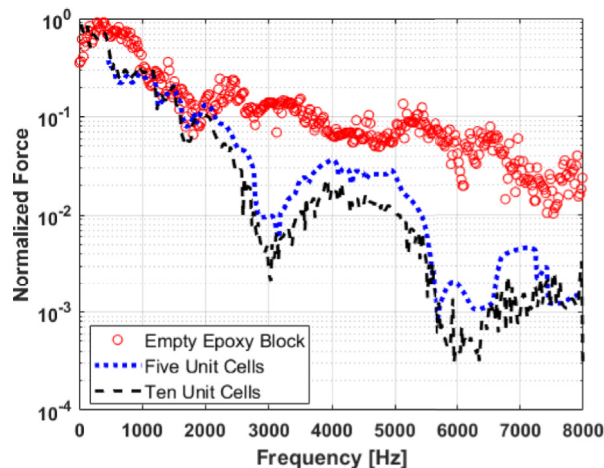


Fig. 12. Experimentally measured frequency domain transmission coefficients for an empty epoxy block (red circles), five unit cell lattice (blue dotted line) and ten unit cell lattice (black dashed). (For interpretation of the references to colour in this figure legend, the reader is referred to the Web version of this article.)

experimentally measured in the time domain by using the force transducer for the two finite lattices with five and ten unit cells and the empty epoxy block for comparison. To ensure the accuracy of the result, the time domain signals are measured and averaged over 50 repeated impacts. Fig. 11 shows the force amplitude for the case with an empty epoxy block for reference.

By calculating the Fast-Fourier transform (FFT) of the averaged time-domain data, the frequency domain amplitudes for two finite lattices consisting of five and ten unit cells as well as an empty epoxy block can be obtained as shown in Fig. 12. Looking back to Figs. 8 and 10, it is apparent that the two band gap/attenuation regions from ~2.5 kHz to ~3.7 kHz and ~5.9 kHz–~6.6 kHz, are also clearly reflected in the experimentally measured force amplitudes for the finite lattices in Fig. 12. Furthermore, it is apparent that the pure passband frequency region of ~3.7 kHz–~5.8 kHz can be significantly attenuated, leading to a broadband energy attenuation region for frequencies above ~2 kHz, which also shows a good agreement with the numerically obtained amplitudes shown in Fig. 10.

5. Conclusion

We have numerically and experimentally demonstrated broadband energy attenuation with a dissipative multi-resonator elastic metamaterial design fabricated from five constituent materials arranged in a layered spherical configuration for the first time. By exploiting the out-of-phase resonant motions of the two internal resonant masses and intrinsic material damping properties of the compliant rubber layers, two strong attenuation regions can be effectively merged into a broadband energy attenuation region. Experimental analysis was carried out to measure the frequency responses of the multi-resonator unit cell to verify the fabrication process of the experimental samples. Finally, 2D numerical analyses were conducted to obtain the dispersion bands and frequency domain transmission amplitudes for a finite lattice. The numerical results were then compared to experimental measurements through finite multi-resonator lattices consisting of five and ten unit cells. Along with good agreement between the analytical, numerical and experimental studies, it has been demonstrated that the dissipative multi-resonator elastic metamaterial design is capable of broadband energy attenuation, which would have a range of practical applications in the field of broadband vibration and/or elastic wave mitigation.

Acknowledgments

This work was supported by the Air Force Office of Scientific Research [Grant No. AF 9550-18-1-0096 with Program Manager Dr. Byung-Lip (Les) Lee].

Appendix A. Supplementary data

Supplementary data related to this article can be found at <https://doi.org/10.1016/j.jsv.2018.08.035>.

References

- [1] V.G. Veselago, The electrodynamics of substances with simultaneously negative values of ϵ and μ , *Sov. Phys. Usp.* 10 (4) (1968) 508–514.
- [2] H.H. Huang, C.T. Sun, G.L. Huang, On the negative effective mass density in acoustic metamaterials, *Int. J. Eng. Sci.* 47 (4) (2009) 610–617.
- [3] Y.Y. Chen, M.V. Barnhart, J.K. Chen, G.K. Hu, C.T. Sun, G.L. Huang, Dissipative elastic metamaterials for broadband wave mitigation at subwavelength scale, *Compos. Struct.* 136 (2016) 358–371.
- [4] S. Krodel, N. Thome, C. Daraio, Wide band-gap seismic metastructures, *Extreme Mech. Lett.* 4 (2015) 111–117.
- [5] Y. Chen, R. Zhu, M. Barnhart, G. Huang, Enhanced flexural wave sensing by adaptive gradient-index metamaterials, *Nat. Sci. Rep.* 6 (2016) 35048.
- [6] O.R. Bilal, M.I. Hussein, Trampoline metamaterial: local resonance enhancement by springboards, *Appl. Phys. Lett.* 103 (111901) (2013) 1–4.
- [7] E. Coffy, T. Lavergne, M. Addouche, S. Euphrasie, P. Vairac, A. Khelif, Ultra-wide acoustic band gaps in pillar-based phononic crystal strips, *J. Appl. Phys.* 118 (214902) (2015).
- [8] Y. Jin, Y. Pennec, Y. Pan, B. Djafari-Rouhani, Phononic crystal plate with hollow pillars connected by thin bars, *J. Phys. Appl. Phys.* 50 (035301) (2017) 8.
- [9] Z. Liu, X. Zhang, Y. Mao, Y. Zhu, Z. Yang, C. Chan, P. Sheng, Locally resonant sonic materials, *Science* 289 (5485) (2000) 1734–1736.
- [10] L. Bonanomi, G. Theocharis, C. Daraio, Wave propagation in granular chains with local resonances, *Phys. Rev.* 91 (2015).
- [11] M.I. Hussein, M.J. Frazier, Metadamping: an emergent phenomenon in dissipative metamaterials, *J. Sound Vib.* 332 (20) (2013) 4767–4774.
- [12] P. Pai, H. Peng, S. Jiang, Acoustic metamaterial beams based on multi-frequency vibration absorbers, *Int. J. Mech. Sci.* 79 (2014) 195–205.
- [13] H. Peng, P. Pai, H. Deng, Acoustic multi-stopband metamaterial plates design for broadband elastic wave absorption and vibration suppression, *Int. J. Mech. Sci.* 103 (2015) 104–114.
- [14] R.L. Harne, Y. Song, Q. Dai, Trapping and attenuating broadband vibroacoustic energy with hyperdamping metamaterials, *Extreme Mech. Lett.* 12 (2017) 41–47.
- [15] Y. Liu, J. Yi, Z. Li, X. Su, W. Li, M. Negahban, Dissipative elastic metamaterial with a low-frequency passband, *AIP Adv.* 7 (065215) (2017) 1–7.
- [16] M.A. Lewinska, V.G. Kouznetsova, J.W. van Dommelen, A.O. Krushynska, M. Geers, The attenuation performance of locally resonant acoustic metamaterials based on generalised viscoelastic modelling, *Int. J. Solid Struct.* 126–127 (2017) 163–174.
- [17] R. Zhu, G. Huang, G. Hu, Effective dynamic properties and multi-resonant design of acoustic metamaterials, *J. Vib. Acoust.* 134 (2012) 031006.
- [18] G. Wang, J. Cheng, J. Chen, Y. He, Multi-resonant piezoelectric shunting induced by digital controllers for subwavelength elastic wave attenuation in smart metamaterial, *Smart Mater. Struct.* 26 (025031) (2017).
- [19] M. Rupin, F. Lemoult, G. Lerosey, P. Roux, Experimental demonstration of ordered and disordered multi-resonant metamaterials for Lamb waves, *Phys. Rev. Lett.* 112 (234301) (2014) 1–5.
- [20] J. Yang, S. Dunatunga, C. Daraio, Amplitude-dependent attenuation of compressive waves in curved granular crystals constrained by elastic guides, *Acta Mech.* 3 (2012) 549–562.
- [21] A. Leonard, C. Daraio, Stress wave anisotropy in centered square highly nonlinear granular systems, *Phys. Rev. Lett.* 108 (2012) 214301.
- [22] E. Kim, J. Yang, Wave propagation in single column woodpile phononic crystals: formation of tunable band gaps, *J. Mech. Phys. Solid.* 71 (2014) 33–45.

- [23] Y. Xu, V.F. Nesterenko, Propagation of short stress pulses in discrete strongly nonlinear tunable metamaterials, *Philos. Trans. R. Soc. A* 372 (2017) 20130186.
- [24] C. Kettenbeil, G. Ravichandran, Experimental investigation of the dynamic behavior of metaconcrete, *Int. J. Impact Eng.* 111 (2018) 199–207.
- [25] F. Bloch, Über die quantenmechanik der elektronen in kristallgittern, *Z. Phys.* 52 (7–8) (1929) 555–600.
- [26] A.O. Krushynska, M. Miniaci, V.G. Kouznetsova, M.G. Geers, Multilayered inclusions in locally resonant metamaterials: two-dimensional versus three-dimensional modeling, *J. Vib. Acoust.* 139 (2) (2017), 024501-024501-4.
- [27] L. Brillouin, *Wave Propagation in Periodic Structures: Electric Filters and Crystal Lattices*, Dover Publications, 2003.